Smart Rocks and Wireless Communication Systems for Real-Time Monitoring and Mitigation of Bridge Scour
(Progress Report No. 2)

Contract No: RITARS-11-H-MST
(Missouri University of Science and Technology)

Ending Period: December 31, 2011

PI: Genda Chen
Co-PIs: David Pommerenke and Rosa Y. Zheng

Program Manager: Mr. Caesar Singh

Submission Date: January 15, 2012

TABLE OF CONTENTS

EXECUTIVE SUMMARY

In the second quarter, three main components were addressed: 1) signal strength of various permanent magnets with a G858 magnetometer, 2) final design and test of a magneto-inductive communication system with small smart rocks, and 3) acoustic communication protocol, implementation, and evaluation.

With the same outer diameter, it was found that solid cylindrical magnets produce a stronger gradient field than ring magnets. For enclosed ferric objects, a hollow sphere and a solid sphere with the same diameter produce the same strength of electromagnetic field. Due to the limited sampling rate of G858 Magnetometer (10 readings per second), the dynamic effects of rapid switching of the dipole of magnets were not observed during various tests. However, the layout directions of magnet rotations significantly influence the measured strength of electromagnetic field since the dipoles of the magnet rotate in different planes.

The design of a magneto-inductive communication system for small smart rocks was being finalized for laboratory tests in the upcoming quarter. Due to limited space in the small smart rocks, pressure sensor was not implemented for laboratory tests. The prototype of the current version V2.4-2.5 has been built and tested in the laboratory. Both hardware and software activities progressed as expected.

An acoustic communication system was implemented with necessary software and hardware. Both transmitter and receiver implementations were discussed in detail in this report. Debugs were done at each step. The screen snap shots of various implementations are presented and demonstrated the successful implementation of the communication system.

Although the technical works completed in the second quarter meet the milestone accomplishment requirements, the actual cumulative expenditure on the RITA part is approximately 50% of the budgeted expenditure. The difference between the accomplished technical work and the actual expenditure is attributed to the fact that one additional position is yet to be filled specifically for this project and two students supported by different sources have helped perform the scheduled work for this project.

I - TECHNICAL STATUS

I.1 ACCOMPLISHMENTS BY MILESTONE

Task 1.1 Optimal Passive Smart Rock – Engineering design and validation of DC magnetic passive smart rocks

Specific Objectives

In the past quarter, measurements of various magnets were characterized for the following purposes: 1) to quantify the size effect of round magnets and compare them with rod magnets with similar size, 2) to qualify the volume effect of round magnets with solid and hollow steel spheres with same size and same weight, and 3) to understand if the speed of rotating magnets changes their maximum field strengths.

Shape and Volume Effects: Ring vs. Rod Magnets and Hollow vs. Solid Magnets

All tests were performed in the same open football field for consistency and for minimum disturbance of above-ground metal objects near the test site. All the magnets tested were manufactured with high grade Neodymium, Grade N45 (12,500 gauss), by the United Nuclear Scientific LLC.

Strength Gradient-Distance Curves for Ring-Shaped Magnets: To determine the gradient strength of ring shaped magnets, the two sensors (C3344 above C3372) of Magnetometer G-858 were set up in a vertical gradient as shown in Figure 1(a). Each magnet was in horizontal plane and laterally flipped over every foot over a distance of 40 ft. The sizes of ring-shaped magnets include ½ in. × 1/8 in. × 1 in. (outer-diameter × inner diameter × length), 1 in. × 1/4 in. × 1 in., and 1 ½ in. × 3/4 in. × 1 in. It can be seen from Figure 1(b) that the largest ring-shaped magnet can be sensed at a distance of 30 ft. To compare the effects of curve and straight rods, field tests were also carried out with the 1 in. × 1/4 in. × 1 in. (outer-diameter × inner diameter × length) ring and a 1 in. × 1 in. (diameter × length) rod magnet. Figure 1(c) shows the test results. Due to its less magnetic materials, the curved (ring) magnet was sensed at half of the measurement distance as compared with the corresponding stright rod. Therefore, the magnetic field of a curved magnet not only depends on the outer diameter but also on the weight of the magnet.

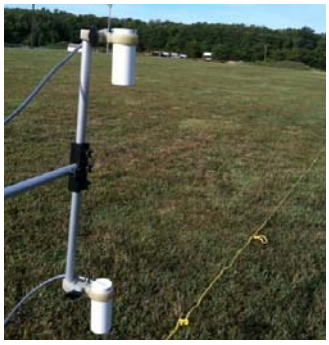

(a) Sensor orientation for vertical gradient measurements

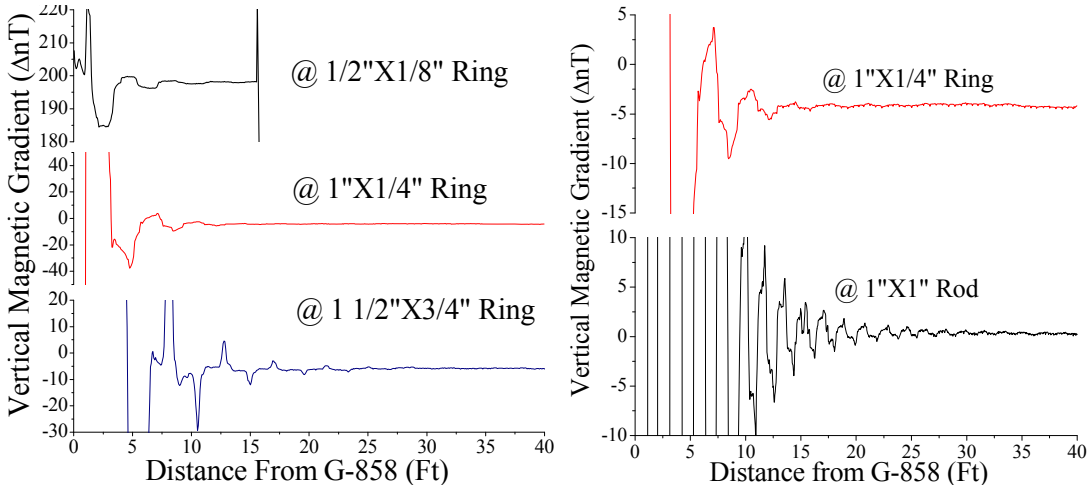

(b) Ring size effect (c) Curve vs. straight rod magnets

Figure 1 Sensor orientation and vertical gradient strength measurements

Strength Gradient-Distance Curves for Hollow and Solid Steel Spheres: To determine whether encasing a smaller magnet with a metal shell increases the gradient strength, two sets of tests were conducted by comparing the magnetic field of hollow steel spheres with that of solid steel spheres. Each test was concluded with two runs, totaling eight runs for the two sets of tests.

The first set of tests was carried out by comparing two steel spheres with the same size (3 in. in outer diameter): hollow vs. solid sphere. The hollow sphere has a 1/8" thick wall. The magnetic field intensity was measured by placing the sensors at one location and moving the spheres away from the sensors in radial direction till it reached 40 ft. Two runs were performed for each sphere and an average of their magnetic field measurements is presented in Figure 2(a). Although the two steel spheres with the same outside diameter weigh quite differently, their magnetic field strength varies little.

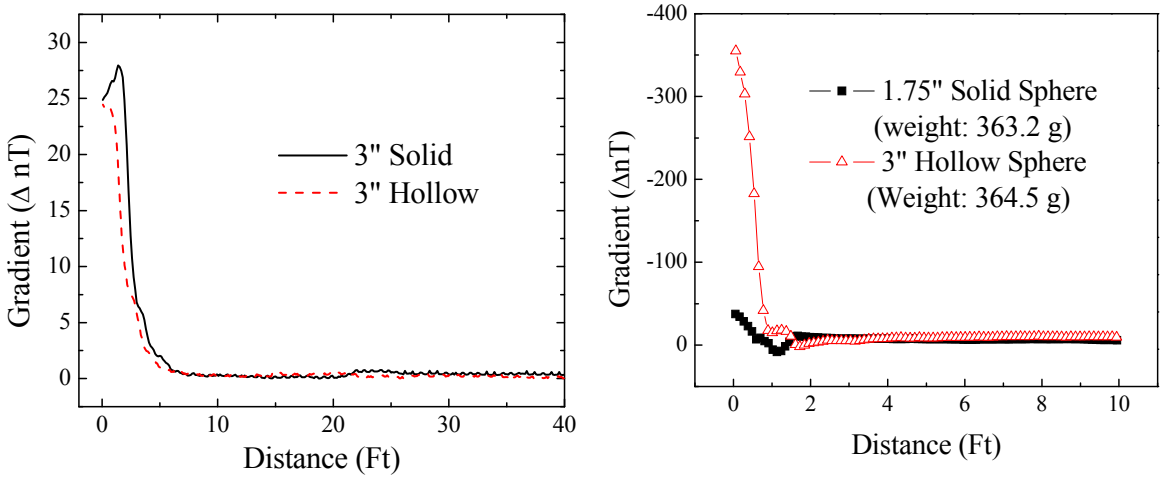

(a) Solid vs. hollow spheres with same size (b) Solid vs. hollow spheres with same weight

Figure 2 Field testing for gradient strengths of solid and hollow steel spheres

The second set of tests was completed in similar way by comparing a solid steel sphere to that of a hollow steel sphere of similar weight (≈364 g). As shown in Figure 2(b), the hollow sphere yielded a significantly stronger magnetic field and can thus be sensed much further.

Rotation Speed Effect

To understand whether the dynamic effect of rotating an magnet can increase the sensitivity of magnetic field strength in application and thus the maximum measurement distance, a series of tests with magnet rotations were conducted at the same test site as for other field tests. The magnetometer was placed five feet away from rotating magnets.

Manual rotation tests: Three magnets with different shapes and sizes were investigated, including a ½ in. × 1 in. (diameter ×length) rod, a 1 in. × 1 in. rod, and a 1 in. × ¼ in. × 1 in. (outer diameter × inner diameter × length) ring. All the magnets were rotated from end to end quickly once in plane, slowly twice in plane, and slowly once out-of-plane. Figure 3(a) shows the results of various magnet shapes and sizes and Figure 3(b) details the measurements for the 1 in. × 1in. rod. It can be seen from Figure 3(a) that the 1 in. × 1 in. rod gave the strongest gradient readings due to additional weights compared to other magnets. The detailed view in Figure 3(b) clearly indicated that, with a sampling rate of 10 readings per second by Magnetometer G-858, the rotating speed of magnets changed little the minimum and maximum field strengths. The dynamic effects of magnet rotation are negligible in application mainly due to the limited sampling rate. However, the layout directions (in-plane vs. out-of-plane) of magnets significantly affected the measured minimum and maximum field strengths as the dipoles of magnets rotated in different planes: horizontal to vertical.

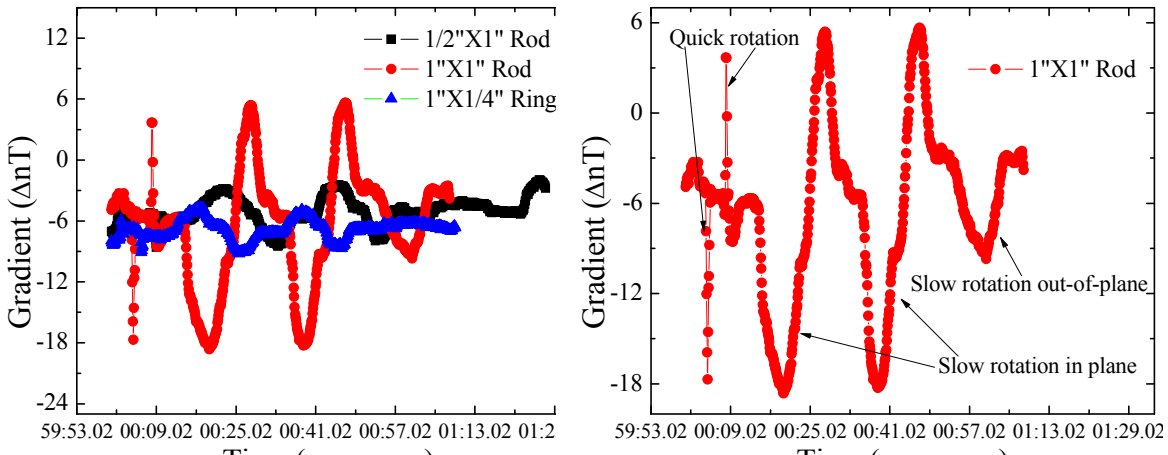

(a) Various magnets shapes and sizes

(b) A 1 in. × 1 in. rod rotating in various speeds

Figure 3 Magnetic gradient vs. time for various magnets at constant distance

Controlled rotation tests: To consistently and accurately evaluate the layout directional effect on the magnetic field detection of magnets, a rotating apparatus was designed to allow for a constant rotation speed (1 rpm) of a magnet. Figure 4(a) displays this device

for a better visualization. The magnetic gradient was measured as the apparatus rotated the ½ in. × 1 in. (diameter × length) magnetic rod. Figure 4(b) shows the results for the magnet rotating in the vertical plane. The test results proved that the layout directions of the magnets influenced the field strength measurements by changing from the minimum to the maximum in sine relation as the dipoles of the magnet rotate in the same vertical plane. In comparison with Figure 3(a), Figure 4(b) also indicated that the maximum strength from the controlled rotation tests appeared to be much higher than that from the manual rotation tests where the critical dipole orientations for the minimum and maximum field strengths may be missed unexpectedly.

(a) Test Setup

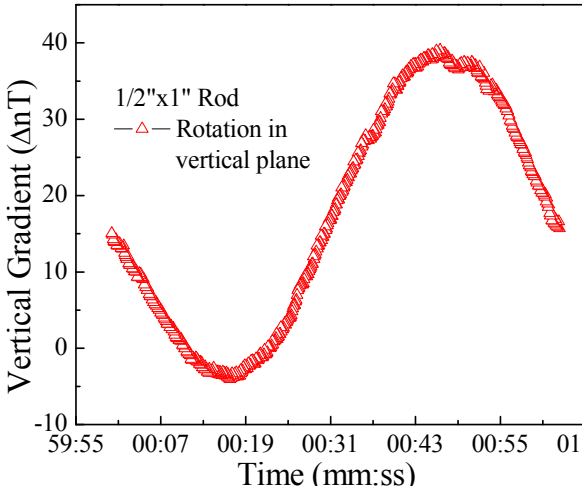

(b) Tests at controlled rotation speed

Figure 4 Gradient strength vs. time of a ½ in. × 1 in. rod magnet

Concluding Remarks

With the same outer diameter, solid cylindrical magnets produce a stronger gradient field than ring magnets. For enclosed ferric objects, however, a hollow sphere and a solid sphere with the same diameter produce the same strength of electromagnetic field. Due to the limited sampling rate of G858 Magnetometer (10 readings per second), the dynamic effects of rapid switching of the dipole of magnets were not observed during various tests. However, the layout directions of magnet rotations significantly influence the measured strength of electromagnetic field since the dipoles of the magnet rotate in different planes.

Task 2.2(a) Magneto-Inductive Communications – Engineering design and validation of magneto-inductive transponders

In the previous quarterly report, a few initial Smart Rock PCB designs up to version 2.3 were discussed. That version was supplied with operational debug features such as multiple jumpers for partial functionality tests, interconnection headers/pads for easy probing and many LEDs for visual status monitoring. To ensure a stable functionality of the test board v2.3, a comprehensive evaluation of the board was performed with special on-board software for the base PIC microcontroller.

The next generation of the Smart Rock PCB, v2.4, was designed in accordance with specifications for laboratory tests of small-scale bridge models. That is, the board is expected in circular shape and should not exceed 2 in. in diameter. The Smart Rock board will be placed in approximately 2.5" diameter spheres, together with a small-size antenna and battery. In addition, another board, v2.5, was recently designed with an alternative circuitry (special IC) used for the transmission part.

The small smart rock board was tested and found to receive clear signals at 10 m distance, which should be sufficient for the small scale test in laboratory. For the large version of smart rocks for field bridge tests, new boards will be designed and built to contain a pressure sensor to determine the depth as well. The small version does not contain it for space reasons.

Smart Rock v2.4-2.5 Technical Details

The Smart Rock v2.4-2.5 board layout is shown in Figure 5 with its main new features.

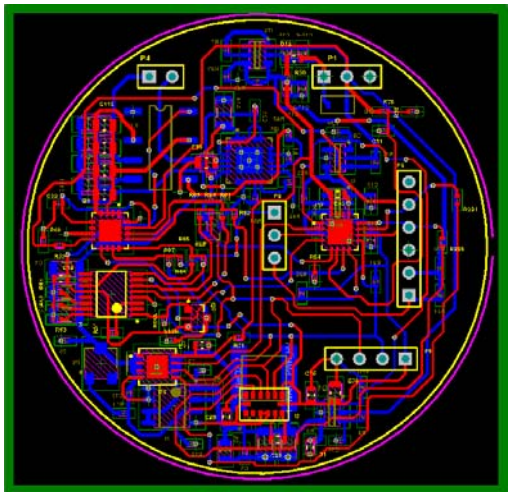

Figure 5 v2.4-2.5 PCB design

- New version of accelerometer/ magnetometer LSM303DLHC-LGA14 (almost twice smaller, less pins, less power, easier to handle)
- Integrated calendar module for long-term timer operation
- Possibility to connect to the receiver module by SPI eliminating I2C-SPI bridge
- Separate tuning capacitor banks for receiving/transmitting coil connection
- Schematic / footprint fixes
- Removed debug features
- H-Bridge/transmission circuit replaced by ATA5276 125 KHz Transmitter IC (v2.5 board)

The new accelerometer/magnetometer sensor (LSM303DLHC-LGA14) was applied in the new Smart Rock PCB. Both accelerometer and magnetometer sensor data are obtained from one unified I2C address accessible by different registers. The previous version required a dual power supply configuration, providing separate 2V and 3V lines. The updated version required only one 3V supply. Therefore, the new sensor occupies a smaller surface area on the board, requires less trace routing (14 pins vs. 28 before), and does not require the separate 2V power supply from the new board. This makes it possible to meet the small size board requirement for the coming laboratory tests.

The new real-time clock and calendar module (PCF8523) provides possibility to use flexible timer (seconds to years delay time) for the Smart Rock boards wake up and data transmission. The time-stamp data can be obtained from this module for accurate interrupt (rock movement) events log arrangement.

The on-board receiver module (AS3930) is the same as that in the previous board but has a new capability to directly communicate with the microcontroller by using the SPI protocol. The PIC microcontroller used in the board can control both SPI and I2C interfaces, which share the same PIC-pins. To ease the on-board PIC programming, the Smart Rock 2.3 had already introduced an I2C-to-SPI bridge IC between the PIC and the receiver module. All the PIC communications on board were performed via the I2C interface. With alternative direct connections and special programming techniques made available on the new board, the PIC microcontroller can independently process SPI and I2C requests. Therefore, the bridge IC in the schematic layout is currently not populated and will be removed from the next generation boards design.

Due to size limitation, some components on the Smart Rock board v2.4-v2.5 were placed on the bottom side of the board. In particular, as shown in Figure 6(a), most of the ICs were placed on the top layer, while all power supply circuits and some modulation/antenna connection elements are mounted from the bottom side as illustrated in Figure 6(b).

The Smart Rock v2.5 board has integrated a special 125 KHz transmitter IC that replaces the equivalent circuit with H-bridge and comparator modules made in house and included in the previous versions. The new transmitter IC allows a further reduction of the board size as needed in the future and provide a more stable and power-effective operation of the board during data transmission. These functions require additional evaluation and tuning. Thus far, the Smart Rock v2.4 board can also use a previously tested transmission circuit.

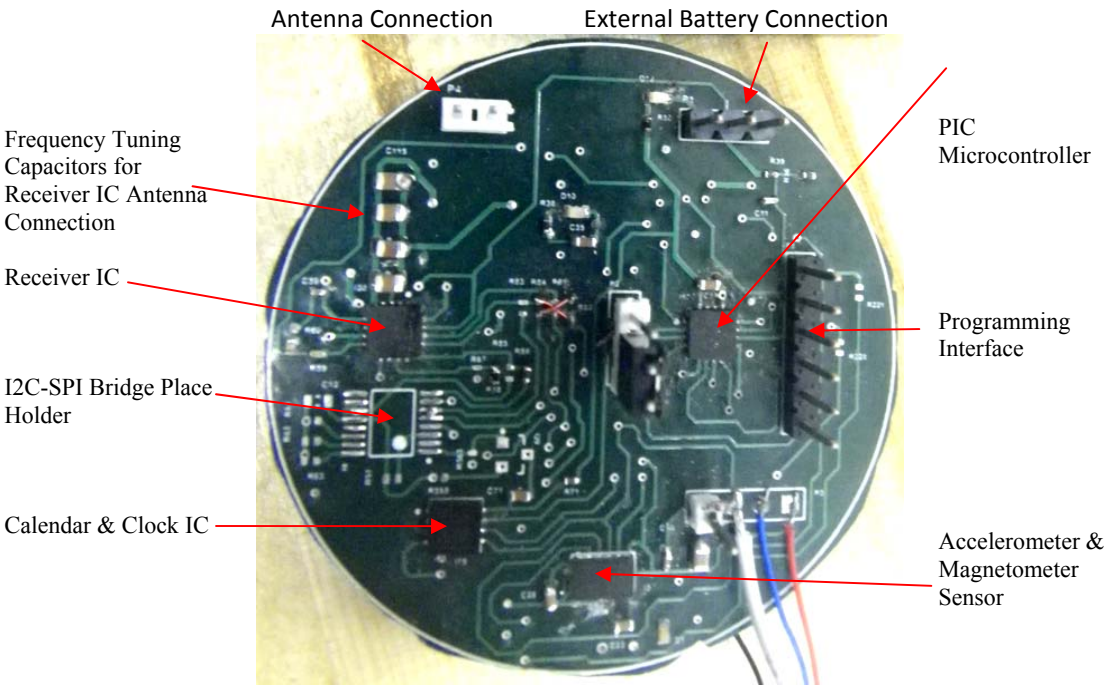

(a) Top view

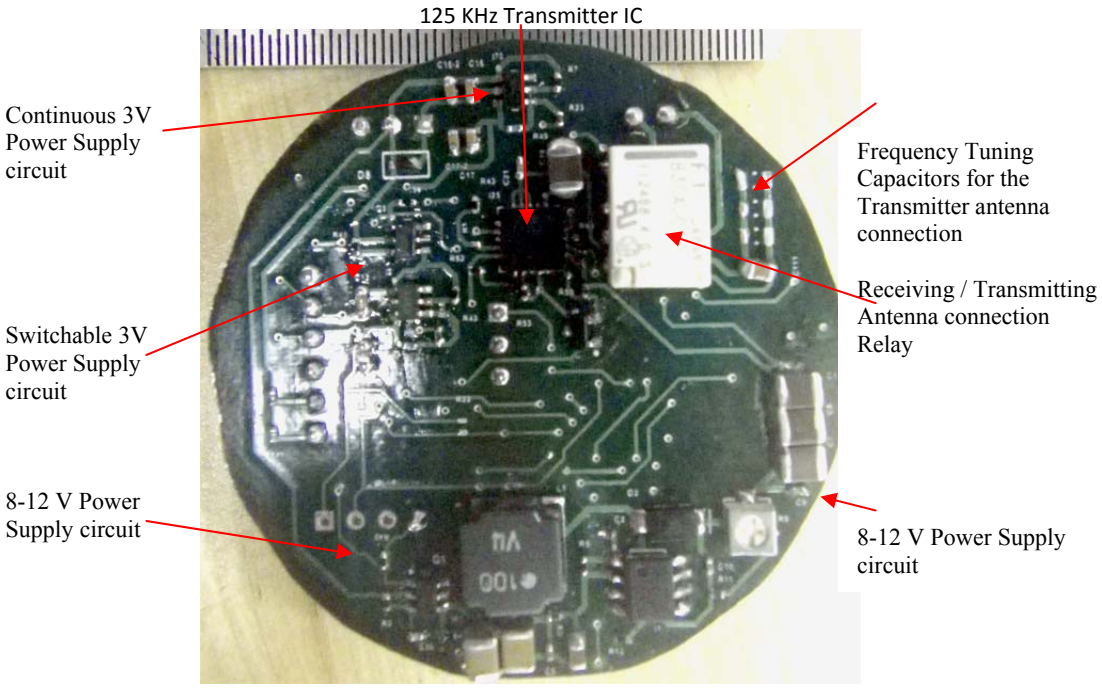

(b) Bottom view

Figure 6 Smart rock board v2.5

Figure 7 shows a schematic view of a packaged smart rock module. It shows a model of a spherical Smart Rock test module with ferrite antenna, Smart rock PCB and battery module placement. The rechargeable battery will be charged by through-hole connection interface at the module wall.

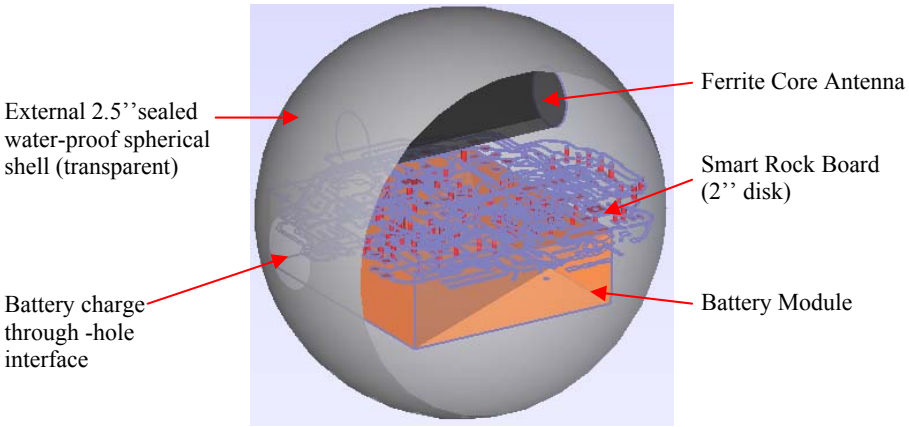

Figure 7 Spherical smart rock module scheme (cut-plane view)

The photo in Figure 8 shows a pair of Smart Rock PCB in operation condition with attached ferrite-core based antennas. Each Smart Rock board has an unique assigned ID, which is used for board data processing and on-demand particular board waking up for data acquisition. The mounted LEDs are for test/debug purposes only, and will be deactivated for practical tests to decrease board current consumption.

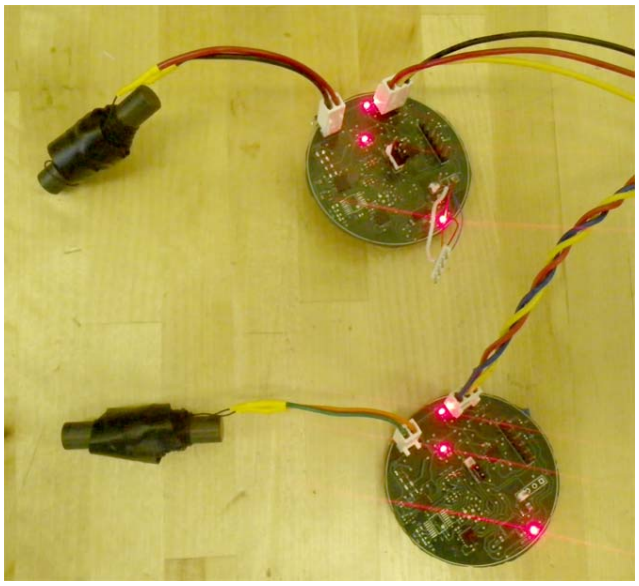

Figure 8 Active smart rock boards v2.4 with attached small-size ferrite-core antennas

Task 2.2(b) Acoustic Communications – Engineering evaluation of acoustic communication systems for bridge scour monitoring

This task report deals with the development and implementation of an acoustic communication system as shown in Figure 9, including transmitter and receiver. During the past quarter, a transmitter at 125 kHz with on-off-keying (OOK) modulation and a receiver at 125 kHz for OOK modulation were designed. The transmitter was implemented with a TMS320C6713 DSK and an AD9765 evaluation board. Samples of the OOK signal at 125 kHz was generated by the TMS320C6713 DSK at the rate of 3 MHz and converted by the AD9765 from digital to analog signal. The receiver was implemented with a TMS320C6713 DSK and an AD7472 evaluation board. The AD7472 was controlled by the TMS320C6713 DSK to sample the input signal at 300 kHz sampling rate, the collected samples were stored at the inner memory of TMS320C6713 and processed by TMS320C6713 to obtain the transmitted signal.

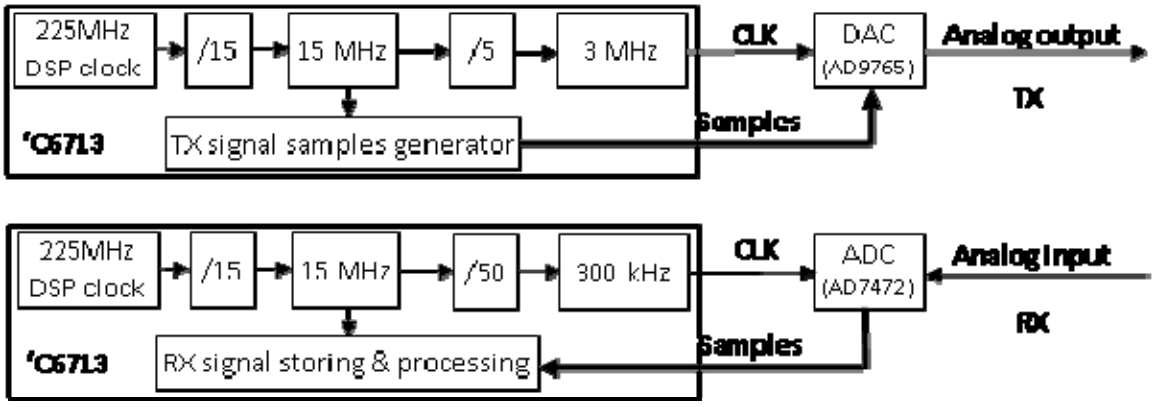

Figure 9 Hardware communication implementation of acoustic communication system

Transmitter Implementation

The implemented transmitter has a carrier frequency of 125 kHz and can thus transmit 24 samples per carrier period at 3 MHz sampling rate. With a data rate of 10 kbps, the number of samples per bit is 300. If a hardware memory of 256 k samples per frame is used, the transmitter can transmit approximately 853 bits in a frame, which is more than required for the smart rocks project.

Acoustic signal generation in mathematics: The on-off-keying modulation scheme allows the transmission of data with value 1, and the block of transmission when the data value is 0. For a carrier frequency of 125 kHz, the carrier period is 8 μs. For a sampling rate of 3 MHz, the sampling period is 1/3 μs. Therefore, considering a zero initial phase, the carrier wave form in terms of time t can be expressed into:

$$Carrier\ (t) = \cos(2\pi f_c t),\ fc=125\ kHz,\ t=0,\ 1/3\ \mu s,\ 2/3\ \mu s,\ \ldots$$

The carrier wave form in terms of sample number can be written as:

$$Carrier\ (sample) = \cos(2\pi\ sample\ f_c/f_s),\ f_s=3\ MHz,\ sample = 0,\ 1,\ 2,\ \ldots$$

The transmitted signal is then generated with

$$S_{TX}(sample) = data(sample) * Carrier(sample),\ sample = 0,\ 1,\ 2,\ \ldots$$

where *data(sample)* is generated with

$$data(sample) = data * [1\ \ldots\ 1]_{1\times 300}$$

since there are 300 samples in each data bit duration at a sample rate of 3 MHz and a data rate of 10 kbps. Here, *data* represent the information bit to be transmitted and are integers in C++ if specified as Boolean type though errors will be generated in the product operation with other parameters. The transmitted signal can be illustrated as shown in Figure 10.

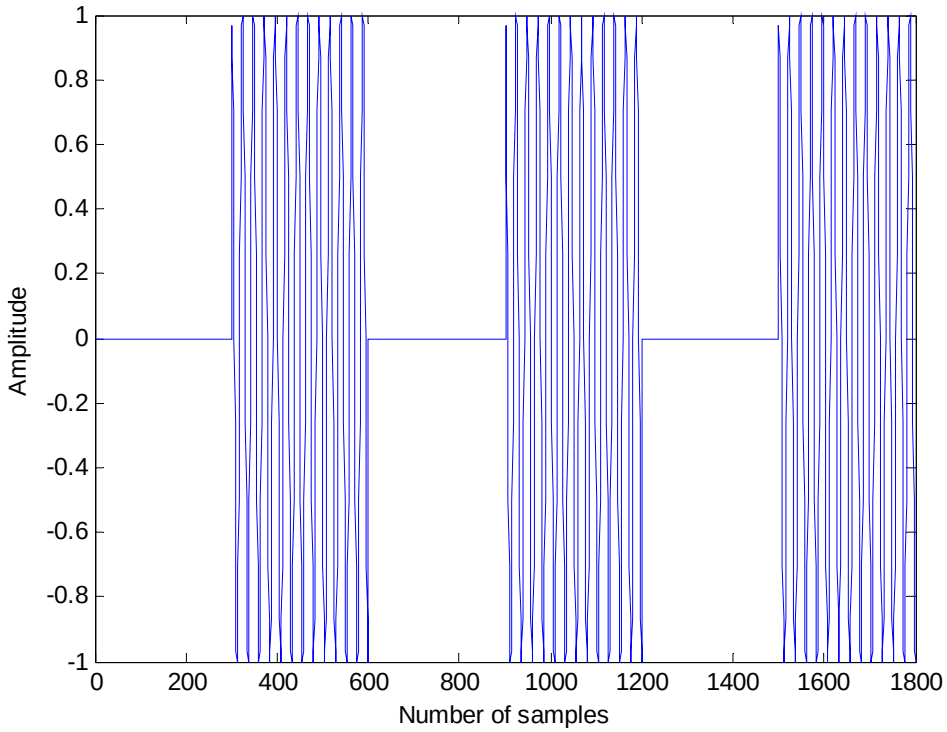

Figure 10 Simulated transmitted signal

Acoustic signal generation on hardware: The AD9765 is a differential current digital to analog converter. In other words, the output of the AD9765 is in the form of two currents $IoutA$ and $IoutB$. For 8 bits of data, from the AD9765 data sheet, the two outputs are $outA = \left(\frac{DACcode}{256}\right) * I_{outFS}$, and $IoutB = \left(\frac{255-DACcode}{256}\right) * I_{outFS}$. Here $DACcode$ is the decimal value of the digital samples and I_{outFS} is the full-scale output current. The maximum value of I_{outFS} for the AD9765 is 20 mA. For this test, I_{outFS} was not scaled in anyway and left at 20 mA. To change these currents into the voltage needed by the transmitter, the DAC evaluation board uses a set capacitors and resistors. The voltage and current are related to the value of the resistor by these simple equations: $V_{outA} = I_{outA} * R_{load}$ and $V_{outB} = I_{outB} * R_{load}$. Here, R_{load} is the load seen by the outputs of the DAC board. In this case, R_{load} = 50Ω was used.

The differential output voltage is $V_{diff} = (I_{outA} - I_{outB}) * R_{load}$. The $DACcode$ can be determined for a specific differential output voltage (V_{diff}), output load (R_{load}) and the full-scale output current (I_{outFS}). That is, $DACcode = \frac{\frac{V_{diff}}{R_{load} * I_{outFS}} + 255}{2}$ or $DACcode = 0, 1, \ldots, 255$. Inputs to the DAC are 8-bit digital words. In this design, the 8 bits are connected to the lower 8 bits of the EMIF data bus.

Hardware setup: A data clock was established for the signal transmitter. The TMS320C6713 was connected to AD9765 that was configured to operate in dual-port mode. An example transmitted signal is presented in Figure 11.

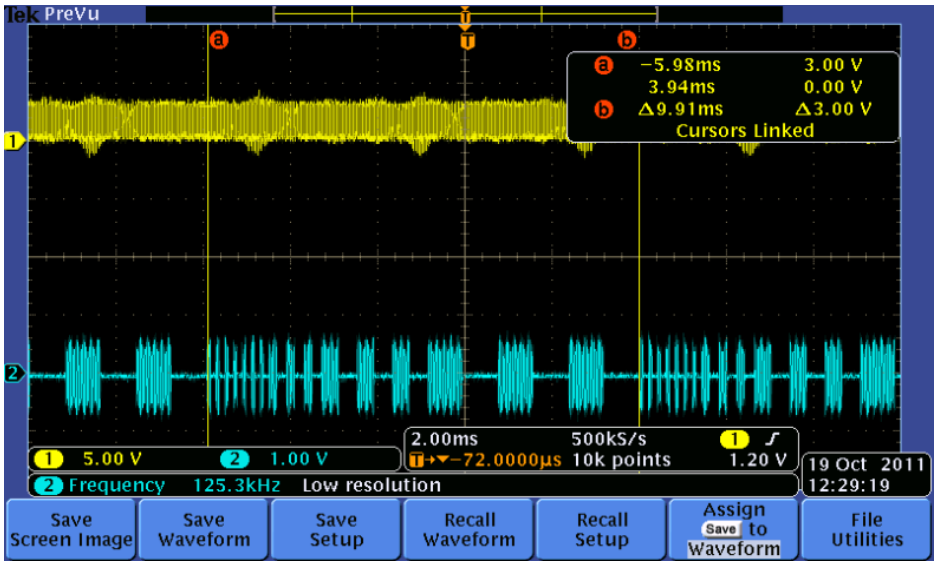

Figure 11 Transmitted signal example

Receiver Implementation

Simulation in Matlab: With a data rate of 10 kbps and sampling rate of 0.3 MHz, a bandpass filter of 100 Hz to 10 kHz was used to avoid some very low frequency noise and out of band interference. An FIR filter was designed using a Hamming window with a filter length of 48. The filter's magnitude and phase responses are shown in Figure 12.

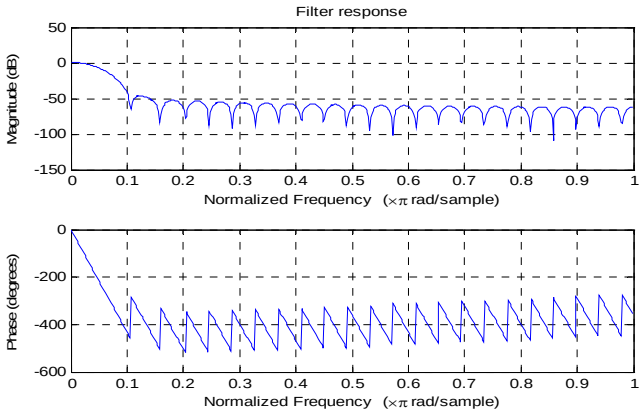

Figure 12 Filter response

Time synchronization: An index code (7-bit Barker-code 1 1 1 0 0 1 0) was introduced for time synchronization between a receiver and a transmitter. Both the simulated received signal and the filtered one (band pass filter output) are given in Figure 13. The data following the index is 1 0 0 1 1 0 1 1 0 0 1. In the detection process, a threshold was first established based on the background noise level, sample signals stronger than the threshold were then detected, and finally time synchronization began from their corresponding time instances. As the time synchronization is completed, the transmitted data can be detected from the received signal with a small processing delay.

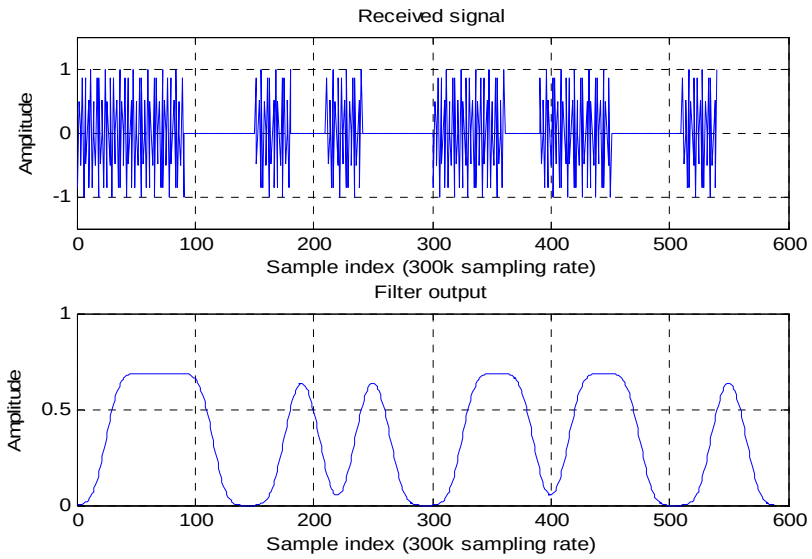

Figure 13 Time synchronization

Implementation on DSK6713 and AD7472

A 15MHz EMIF clock was set for the EMIF read setup = 2, read strobe = 46, and read hold = 2, to achieve a sampling rate of 0.3 MHz. In receiver design, the ARE signal (6713DSK-J4-pin73) was used as input to the AD7472 CONVST, which is by default in the sleep-wake up mode (it is satisfactory because of the low sampling rate requirement, 0.3 MHz). The AD7472 t_{WAKEUP} is typically 1 μs. Therefore, as long as the read setup and the read strobe are each long enough to exceed 1 μs + 14 AD7472 clock cycles (analog to digital conversion time), the digital samples on the data bus of AD7472 can be received with high fidelity. The AD7472 evaluation board provides a 25 MHz clock, which can be used as the AD7472 CLK IN signal. As such, the read setup plus read strobe should not be less than 1.56 μs (0.56 from 14 AD7472 clock cycles at 25MHz). Since the AD7472 $\overline{CS}$ and $\overline{RD}$ was tied to low, the signal sample data becomes available on the data bus immediately after the AD7472 is waken up and converts the analog signal to digital.

Figure 14 shows three waveforms demodulated from the signal carrier based on a simulated raw sample signal. They are (a) the received sample waveform that represents the absolute value of the raw samples, (b) the band pass filter output waveform, and (c) the clipped waveform at the threshold level.

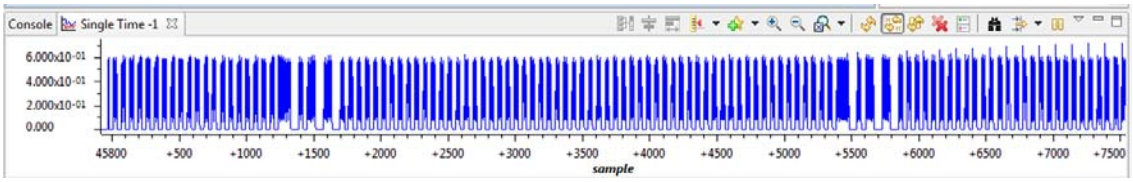

(a) Received sample waveform

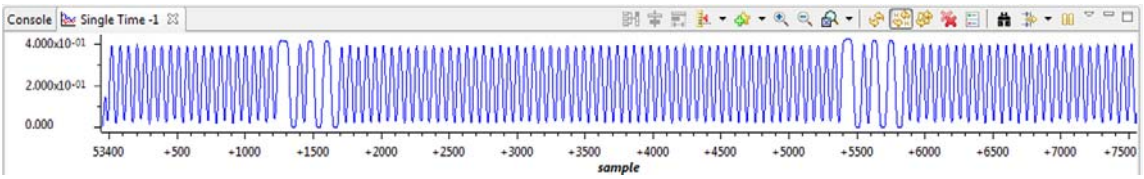

(b) Band pass filter output waveform

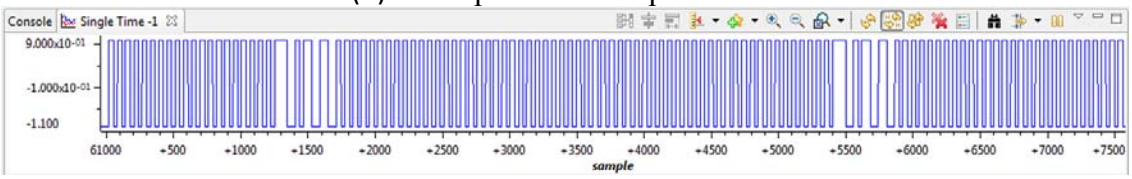

(c) Clipped waveform at the threshold level

Figure 14 Three waveforms when demodulated form the carrier

I.2 PROBLEMS ENCOUNTERED

During the second quarter of the project, no unexpected technical problem was encountered.

The previous identified post-doctoral fellow recently took another job. As such, we are still short of one post-doctoral fellow for this project. Two Ph.D. students who were supported from other sources continued to be asked to participate in this project and keep technical work moving forward as scheduled.

I.3 FUTURE PLANS

Three subtasks will be executed during the next quarter. A brief description of various activities in each subtask is described below:

Task 1.1 Design, fabricate, and test in laboratory and field conditions DC magnetic sensors with embedded steel in Dodecahedron shape or magnets aligned with the earth gravity field. Summarize and document the test results and the performance of passive smart sensors.

Built on the previous work, magnets will be embedded inside concrete blocks in various shapes. Their effectiveness in providing sensitive magnetic field measurements will be systematically characterized.

Task 1.2 Research, summarize, and document the degree of potential steel interferences to magnetic measurements. Investigate ways to compensate the interference effect and develop a rock localization technique.

Laboratory work will begin to test potential interference of ferrous objects on magnetic field measurements.

Task 2.1 Design, fabricate, and test in laboratory and field conditions active smart rocks with embedded controllable magnets or with embedded electronics. Summarize and document the test results and the performance of active smart rocks.

The design of active smart rocks with controllable magnets is currently under way. The test results will be reported during the following quarterly report.

Task 2.2(a) Design, fabricate, and test in laboratory and field conditions magneto-inductive transponders. Summarize and document the test results and the performance of transponders.

The magneto-inductive communication system V2.4-2.5 will be packaged for laboratory tests. New magneto-inductive communication system will be designed and tested with full size smart rocks. Small scale versions will be tested in a laboratory, such as the Hydraulic Engineering Laboratory at Turner-Fairbank Highway Research Center, Federal Highway Administration.

In addition, pressure sensor will be integrated into the large version of smart rocks and their communication system.

Task 2.2(b) Research, summarize, and document current underwater acoustic transmission practices and required modifications for bridge scour monitoring.

In the following quarter, the acoustic communication system with transmitter and receiver will be refined. A multi-receiver system will then be built and tested with capability of smart rock localization. In this case, multiple transducers / hydrophones are distributed to different locations for TDOA estimation. The smart rocks will be located using the TDOA fusion and the assistance of pressure sensor in smart rocks, which provides the elevation information of the smart rocks.

Task 3.2 Plan and execute the field validation tasks of various prototypes. Analyze the field performance of smart rocks and communication systems.

As prototype smart rocks are being designed and built, field test plan will be developed during the following report.

II – BUSINESS STATUS

II.1 HOURS/EFFORT EXPENDED

The planned hours and the actual hours spent on this project are given and compared in Table 1. In the second quarter, the actual hours are approximately 46% of the planned hours due to short of staff appointed on this particular project. That is, the actual cumulative hours are approximately 35% of the planned hours. The cumulative hours spent on various tasks by personnel are presented in Figure 15.

Table 1 Hours Spent on This Project

	Planned		Actual	
	Labor Hours	Cumulative	Labor Hours	Cumulative
Quarter 1	752	752	184	184
Quarter 2	752	1504	345	529

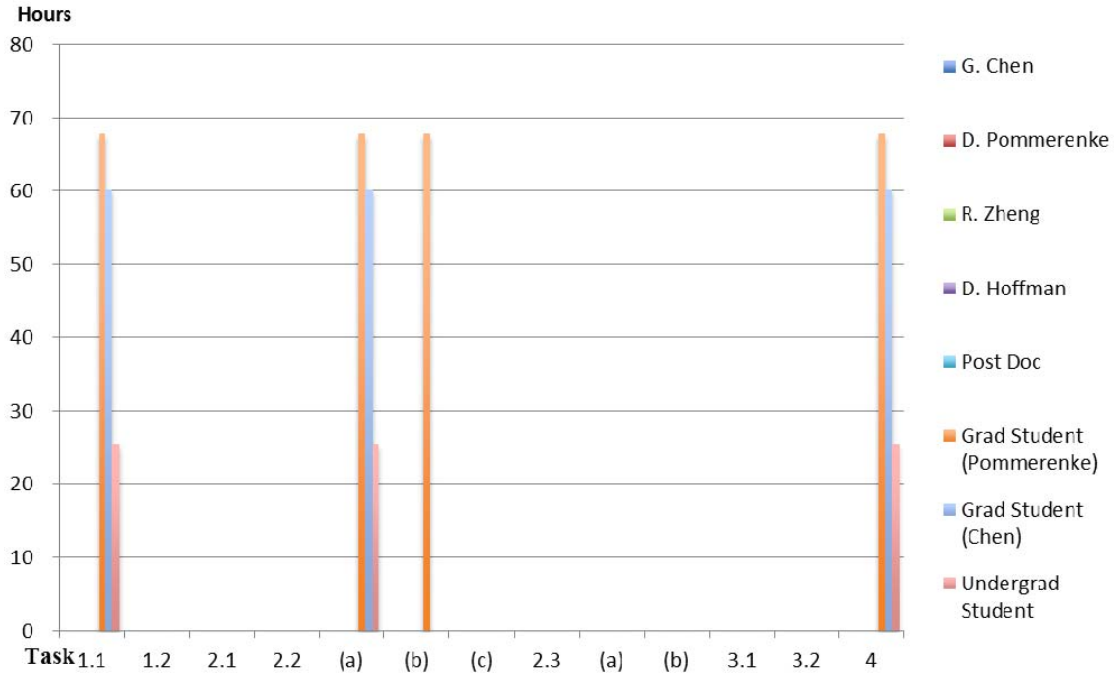

Figure 15 Cummulative hours spent on various tasks by personnel

II.2 FUNDS EXPENDED AND COST SHARE

The budgeted and expended RITA funds in each quarter are compared in Figure 16. Approximately 50% of the budget has been spent during the second quarter. The actual cumulative expenditures from RITA and Missouri S&T are compared in Figure 17. It can be seen from Figure 17 that the expenditure from RITA is approximately 76% of that

from the Missouri S&T. Their ratio (RITA to Missouri S&T) is less than 1.0, which meets the minimum match fund requirement.

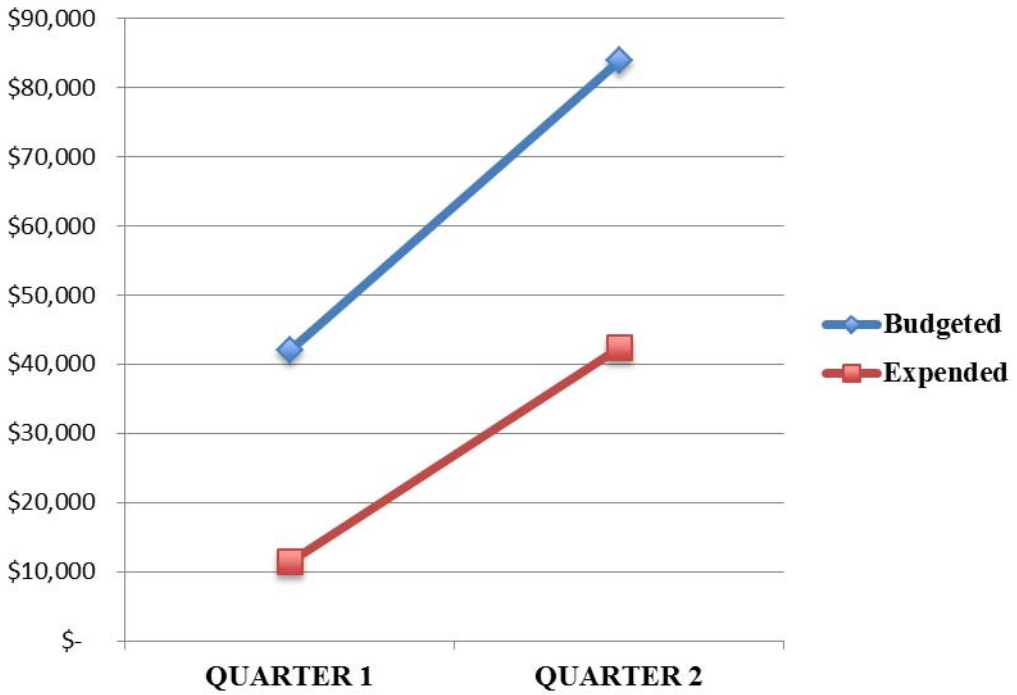

Figure 16 RITA budget and expenditure comparison in every quarter

Figure 17 Cummulative expenditures by sponsor